



Micro-integrated diode laser modules enabling mode-hop-free tuning and long-term frequency stabilization

JANPETER HIRSCH,^{1,*} MARTIN GÄRTNER,¹ NORA GOOSSEN-SCHMIDT,¹ SRIRAM HARIHARAN,^{1,2} SIMON KUBITZA,¹ TAMUKANASHE MUSENGEZI,¹ MAX SCHIEMANGK,¹ CHRISTOPH STÖLMACKER,¹ CHRISTOPH TYBORSKI,^{1,3} AND ANDREAS WICHT¹

¹Ferdinand-Braun-Institut (FBH), Gustav-Kirchhoff-Str. 4, 12489 Berlin, Germany

²Currently at eleQtron GmbH, Heeserstr. 5, 57072 Siegen, Germany

³Currently at CryLaS Crystal Laser Systems GmbH, Ostendstr. 25, 12459 Berlin, Germany

*janpeter.hirsch@fbh-berlin.de

Received 27 June 2025; revised 17 September 2025; accepted 22 September 2025; posted 23 September 2025; published 14 October 2025

We present a robust and compact hybrid micro-integrated ECDL-MOPA laser module developed for quantum technology applications. The laser module operates at a wavelength of 767 nm with a PM fiber-coupled output power of up to 360 mW. The module's dimensions and mass are $139 \times 80 \times 33 \text{ mm}^3$ and 800 g, respectively. We demonstrate a mode-hop-free frequency tuning range of 22 GHz using a control loop that derives its error signal from the spectroscopy of the frequency-selective element. This tuning range can be extended beyond 100 GHz by implementing a cascaded control loop. The free-running laser features a technical linewidth of approximately 165 kHz at 1 ms and a minimum overlapping Allan deviation of $\sigma(\tau = 6 \text{ s}) = 6 \cdot 10^{-10}$. A reduction of the frequency drift by up to one order of magnitude [i.e., from $\sigma(\tau = 10^5 \text{ s}) = 10^{-7}$ to $\sigma(\tau = 10^5 \text{ s}) = 7 \cdot 10^{-9}$] was achieved at averaging times exceeding 500 s by stabilizing the laser to its internal volume holographic Bragg grating. © 2025 Optica Publishing Group. All rights, including for text and data mining (TDM), Artificial Intelligence (AI) training, and similar technologies, are reserved.

<https://doi.org/10.1364/AO.571474>

1. INTRODUCTION

Quantum sensors are already surpassing classical devices in precision and sensitivity, making them indispensable tools for a wide range of applications, including inertial navigation [1], geophysics [2], sensing of magnetic [3] and electric fields [4], time keeping [5], and fundamental physics [6,7]. Among the key components of portable quantum sensors are compact and robust diode laser modules, which exhibit narrow emission linewidths, high output powers, and wide, independent tuning of emission frequency and output power.

Laser modules based on the master oscillator power amplifier (MOPA) concept [8–13] are popular light sources for quantum technology applications due to their intrinsically independent tuning capabilities. Furthermore, by employing two distinct semiconductor chips, a separate optimization of the spectral and power characteristics of the laser module can be achieved: highly coherent radiation is generated in the seed laser chip, and the output power is enhanced in a semiconductor optical amplifier (SOA) chip. Extended cavity diode lasers (ECDLs) are among the most widely used sources of narrow linewidth emission in atomic physics applications [9,10,14,15] and are a

natural choice as the master oscillator. ECDLs can be combined with ridge waveguide amplifiers (RWAs) or tapered amplifiers (TAs) to boost their optical output powers, building a MOPA structure. RWAs feature high output powers, excellent beam quality, and low internal back-coupling when the waveguide is tilted, whereas TAs are superior with respect to amplification at the expense of worse beam quality.

Compact and robust ECDL-MOPA modules emitting highly coherent light with a technical linewidth of 13 kHz at 1 ms time scales and with optical output powers of 570 mW at a wavelength of 1064 nm have already been demonstrated [10]. However, a potential drawback of ECDL-based laser modules is the occurrence of mode hops when tuning the frequency by means of the injection current into or the temperature of the ECDL chip, limiting the continuous frequency tuning range to a couple of GHz.

Extending the mode-hop-free frequency tuning range is possible by tuning the optical resonator length and the center frequency of the frequency-selective element at the same time. Such synchronous tuning was already demonstrated over a frequency range of 27.5 GHz [16]. However, since active synchronization was omitted, continuous calibration remains

necessary, and environmental disturbances can disrupt the synchronization.

The commercial continuously tunable laser (CTL) from Toptica employs an active feedback loop with mechanical actuators (motor and piezo) to synchronize the tuning of the optical resonator length and the frequency-selective element of the ECDL [17], achieving up to 120 nm of mode-hop-free tuning [18]. Similar approaches using active feedback on mechanical actuators for synchronized tuning have been demonstrated in other tunable laser systems as well [19–22]. That said, the reliance on mechanical components for frequency tuning, combined with its relatively large footprint ($370 \times 150 \times 90 \text{ mm}^3$), makes it unsuitable for use in harsh or unstable environments, such as mobile platforms in the field or space-based applications.

In this paper, we present our next-generation robust and compact hybrid micro-integrated ECDL-MOPA modules, which contain no movable parts. We describe our approach to overcoming the limitations of previous designs, achieving an extended mode-hop-free frequency tuning range and an internally stabilized emission frequency. The versatile module platform, in principle, allows for realizing laser modules at any wavelength as long as suitable (electro-)optical components are available, with modules already realized at 689, 767, 780, and 794 nm. Here, we present the electro-optical performance of a module emitting at a wavelength of 767 nm. Laser modules emitting at 767 nm are of particular interest for potassium-based quantum technology experiments, where they are employed for laser cooling, coherent manipulation, detection, and the stabilization of reference lasers [23,24].

This paper is organized as follows: Section 2 describes the structure of the ECDL-MOPA module. In Section 3, the electro-optical performance of the module is evaluated in detail, starting with the power and frequency tuning behavior in Subsections 3.A and 3.B. In Subsections 3.C and 3.D, the spectral stability and purity of the module are examined, respectively. The results of this paper are summarized in Section 4 with a short outlook on future developments.

2. HYBRID MICRO-INTEGRATION OF THE ECDL-MOPA MODULE

Figure 1 shows a photograph of the next-generation hybrid micro-integrated ECDL-MOPA module. All optical and electro-optical components are located on a nickel-coated metallic micro-optical bench (MIOB). The MIOB is composed of a sintered molybdenum–copper ($\text{Mo}_{70}\text{Cu}_{30}$) alloy with high thermal conductivity ($>185 \text{ W/mK}$ at 20°C) and a coefficient of thermal expansion (CTE), which matches the CTE of the GaAs master-oscillator and power-amplifier chips, effectively minimizing thermally induced stress. The non-magnetic MoCu alloy allows for easy mechanical processing with standard equipment, enabling, for instance, the erosion of four solid joints into the MIOB, which ensures mechanical decoupling of the MIOB from the housing [25]. High temperature stability as well as temperature tuning capabilities of the MIOB are achieved by connecting four Peltier elements to the housing and with flexible thermal straps to the MIOB's bottom side. The top side of the MIOB hosts printed circuit boards (PCBs), Peltier elements, and optics, adhesively bonded either directly to the MIOB

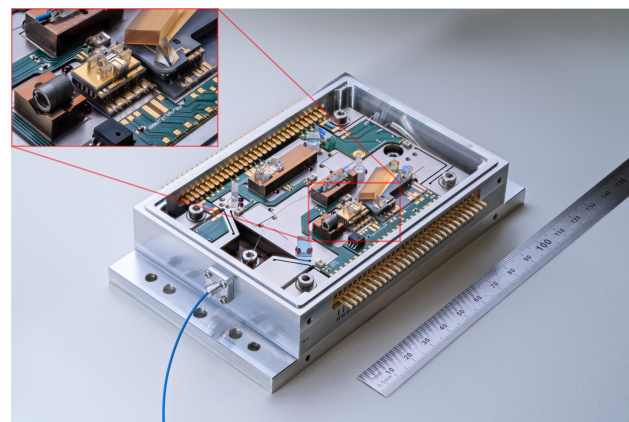


Fig. 1. Photograph of the PM fiber-coupled ECDL-MOPA laser module. The inset shows a close-up of the laser cavity. The module dimensions ($139 \times 80 \times 33 \text{ mm}^3$) are indicated by the ruler shown for scale.

or to additional MoCu spacers. High-precision ruby spheres, placed in milled conical recesses, serve as mechanical stops for accurate component positioning. The MIOB is enclosed by an aluminum housing with two 30-pin headers and an optical fiber feedthrough. The electrical connections from the PCBs to the pin headers, to the Peltier elements, to the semiconductor chips, and to the sensors are established by gold bond wires. The module features dimensions of $139 \times 80 \times 33 \text{ mm}^3$ and a mass of 800 g, making it suitable for various applications in the field or in space.

Figure 2 illustrates the master-oscillator power-amplifier concept of the laser module. The ECDL is composed of a 2 mm long ridge waveguide laser chip and an external volume holographic Bragg grating (VHBG), which acts as the frequency-selective element. The cavity is formed between the 30% reflection-coated laser chip's facet, from which the light is emitted, and the VHBG. The intra-cavity facet of the laser chip is anti-reflection (AR) coated to prevent the excitation of parasitic Fabry–Perot modes. An aspheric micro-lens ($f = 0.55 \text{ mm}$) focuses the optical beam into the VHBG, which is operated in Littrow configuration with the beam propagating parallel to the grating vector to ensure robust coupling [26]. The custom-made VHBG, manufactured by Optigrate, was optimized for a stable single longitudinal laser mode operation and features a 7.6 GHz full width half maximum (FWHM) bandwidth and a 60% peak diffraction efficiency. Both the laser chip and the VHBG are placed on separate custom-made Peltier elements with built-in negative temperature coefficient (NTC) thermistors for temperature stabilization and tuning. An intra-cavity pick-off point is created by tilting the VHBG's facet by 45° with respect to the incident optical beam and by coating the VHBG's intra-cavity facet with 3% reflectivity, enabling the measurement of the intra-cavity optical power incident on the VHBG with a photodiode (PD-I). The optical power transmitted through the VHBG is measured by a second photodiode (PD-T). Both photodiodes are embedded within the Peltier element beneath the VHBG to minimize noise from scattered light. The photodiodes are illuminated via reflection prisms, which are positioned on top of the Peltier element.

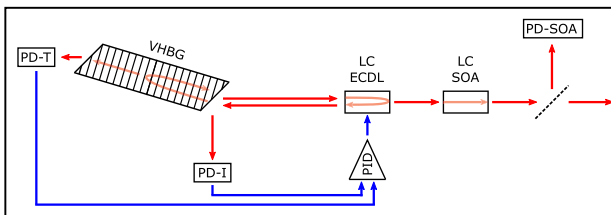


Fig. 2. Schematic diagram of the MOPA concept. Abbreviated components: PD-T, PD-I, and PD-SOA, photodiodes for monitoring transmitted, incident, and SOA output power; VHBG, volume holographic Bragg grating; LC ECDL, laser chip of the extended cavity diode laser; LC SOA, laser chip of the semiconductor optical amplifier; PID, proportional-integral-derivative controller.

Two aspheric micro-lenses ($f = 1.45$ mm) and two micro-mirrors are used to couple the laser beam efficiently into the RWA chip. An optical micro-isolator is integrated directly behind the ECDL's collimating lens. With 60 dB isolation, it minimizes optical feedback into the ECDL, which is known to increase the frequency noise [27], thereby also mitigating a potential source of spectral instability. Depending on the module's wavelength, a commercial or self-developed [28,29] optical micro-isolator is used. The amplified laser beam is collimated with an aspheric micro-lens ($f = 2.00$ mm) and coupled into a polarization-maintaining (PM) single-mode fiber using two micro-mirrors and a custom-made fiber collimator. To ensure a high polarization extinction ratio of the fiber-coupled light, a polarizing beam splitter (PBS) is placed in front of the fiber collimator. The fiber is actively aligned to the PBS to optimize the coupling with respect to the desired polarization axis. A third photodiode (PD-SOA) is placed behind the first redirection mirror in the path between the SOA and the fiber collimator to monitor the optical output power of the SOA.

3. ELECTRO-OPTICAL CHARACTERIZATION OF THE ECDL-MOPA MODULE EMITTING AT 767 NM

The electro-optical performance of the ECDL-MOPA module was evaluated at its designated working point, defined by the injection currents into the ECDL and SOA chips ($I_{ECDL} = 124$ mA and $I_{SOA} = 750$ mA) and by the temperature settings for the heat sink ($T_{HS} = 20.0^\circ\text{C}$), MIOB ($T_{MIOB} = 24.5^\circ\text{C}$), VHBG ($T_{VHBG} = 30.5^\circ\text{C}$), and ECDL chip ($T_{ECDL} = 24.0^\circ\text{C}$). This working point ensures that the laser is running with the emission frequency required for exciting the ${}^{39}\text{K}$ D2 ground-state crossover transition ($\nu = 391.016230$ THz). This specific frequency was chosen because (i) it lies at the center of several frequencies required for cold-atom potassium experiments [24] and (ii) it is commonly used for stabilizing reference lasers in such experiments [23,24]. In some characterization measurements, changes in the measurement environment (ambient temperature, pressure, and relative humidity) might result in slightly different emission frequencies or an adjusted operating point.

Laser diode controllers LDC501 and LDC502 from Stanford Research Systems (SRS) were used to drive the injection current into the ECDL and SOA chips, respectively. To reduce

the injection current noise in spectral stability measurements in Subsection 3.C, the current drivers were operated in low-bandwidth mode. Additionally, home-built passive, second-order low-pass filters with cutoff frequencies of approximately 100 Hz were employed. The Peltier elements of the module and the heat sink were controlled by a single multi-channel PTC10 temperature controller from SRS.

A. Power Tuning

To facilitate independent frequency and power tuning of the ECDL-MOPA laser module, the SOA chip is operated in saturation, reducing the influence of I_{ECDL} , which is used to tune the frequency, on the output power. To investigate the parasitic power tuning via the ECDL's injection current, we swept I_{ECDL} bidirectionally between 35 and 200 mA and measured the fiber-coupled output power with an integrating sphere from Thorlabs (S142C). The recorded data are displayed in Fig. 3. The ECDL's threshold current of 40 mA marks the point where the output power rises considerably from a constant level of 170 mW, which originates from the SOA's amplified spontaneous emission (ASE). The curve exhibits multiple power jumps with a parabolic shape between jumps, resulting from frequency-dependent variations in the VHBG's diffraction efficiency. After the first mode-hop, the influence of I_{ECDL} on the output power decreases noticeably, owing to saturation of the SOA chip.

To avoid mode-hops, parabolic power variations, and excessive frequency shifts, the optical output power of the module is primarily tuned by adjusting the injection current of the SOA chip. The power tuning characteristics of I_{SOA} were examined analogously to I_{ECDL} in the range of 0 and 800 mA. The results of this measurement are shown in Fig. 4. Below around 100 mA, the SOA chip effectively acts as an absorber. Above 100 mA, the output power increases linearly with a slope efficiency of 0.5 mW/mA. At approximately 600 mA, the slope efficiency decreases, indicating thermal rollover [30] and potential thermal lensing effects [31], reducing the fiber coupling efficiency.

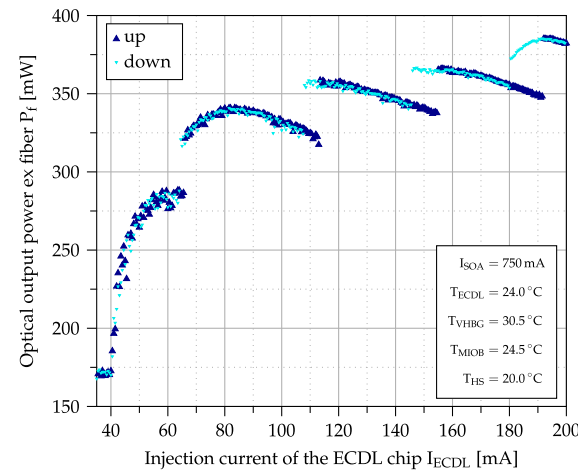


Fig. 3. Fiber-coupled optical output power P_f of the ECDL-MOPA laser module as a function of the injection current of the ECDL I_{ECDL} .

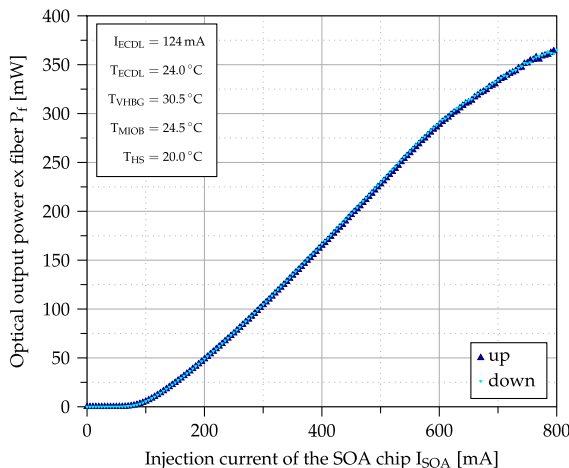


Fig. 4. Fiber-coupled optical output power P_f of the ECDL-MOPA laser module as a function of the injection current of the SOA chip I_{SOA} .

B. Frequency Tuning

Depending on the requirements for tuning speed, tuning range, parasitic amplitude tuning, and mode-hop-free operation, the emission frequency of the laser is tuned by either changing I_{ECDL} , T_{ECDL} , T_{MIOB} , or T_{VHBG} or a combination of them. The first three actuators directly affect the emission frequency by changing the optical path length of the laser resonator. T_{VHBG} influences the center frequency of the frequency-selective element, which determines the longitudinal mode and thus the continuous frequency tuning range.

The frequency tuning behavior of I_{ECDL} was investigated by sweeping the injection current from 35 to 200 mA and back to 35 mA in steps of 0.5 mA. The optical emission frequency was measured with a wavemeter (HighFinesse WS7-60) at every step after a relaxation time of a couple of seconds. The data recorded for injection currents above the threshold current of 40 mA are shown in blue in Fig. 5. An almost linear, continuous mode-hop-free frequency tuning range of 5–6 GHz is observable. At the operating point, the tuning coefficient is approximately -165 MHz/mA . The origin of the non-linearity is most likely amplitude-phase coupling initiated by a change in diffraction efficiency of the VHBG. When scanning the injection current up and down, a mode-hop hysteresis becomes evident, most likely owing to spatial [32] and/or spectral [33] hole burning in the active region, which suppresses adjacent longitudinal modes. Similar curves were measured when tuning T_{ECDL} and T_{MIOB} , with tuning coefficients of -7.8 and -2.1 GHz/K , respectively. In practice, I_{ECDL} tuning is the preferred method for frequency control, since it provides fast response with minimal impact on output power, while T_{ECDL} tuning offers slower but still reliable adjustment. T_{MIOB} , in contrast, has limited leverage and a large time constant and is therefore mainly suited for long-term stabilization rather than active frequency sweeps.

Following the same approach, the frequency tuning behavior of T_{VHBG} was examined in a temperature range of 20°C – 40°C in steps of 0.1°C . A 65 GHz frequency tuning range was achieved, as shown in green in Fig. 5. However, the frequency tuning exhibits a step-wise behavior dominated by mode-hops, with only small frequency changes occurring between the mode-hops. The reason for these small frequency changes is

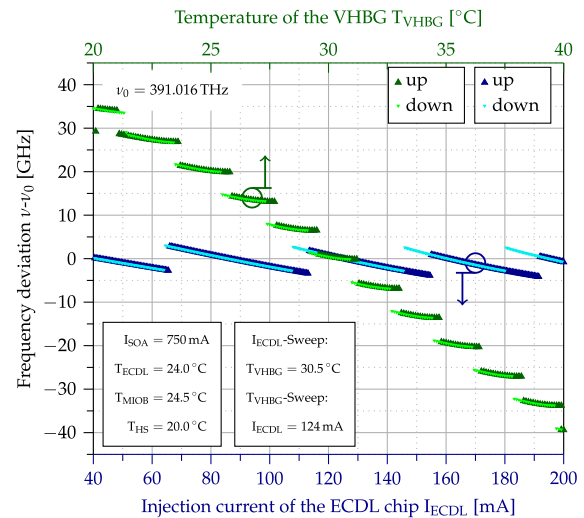


Fig. 5. Optical emission frequency of the ECDL-MOPA laser module v as a function of the injection current of the ECDL I_{ECDL} (blue) and the temperature of the VHBG T_{VHBG} (green).

Table 1. Frequency Tuning Coefficients of the Actuators in the ECDL-MOPA Laser Module

Actuator	Tuning Coefficient
Injection current of the ECDL chip I_{ECDL}	-165 MHz/mA
Temperature of the ECDL chip T_{ECDL}	-7.8 GHz/K
Temperature of the MIOB T_{MIOB}	-2.1 GHz/K
Temperature of the VHBG T_{VHBG}	-3.7 GHz/K (stepwise)
Injection current of the SOA chip I_{SOA}	125 kHz/mA
Temperature of the heat sink T_{HS}	-23 MHz/K

presumably an asymmetric mounting of the VHBG on the Peltier element, resulting in an increasing resonator length of the ECDL and thus a decreasing emission frequency with rising temperatures, in addition to the aforementioned non-linearity due to amplitude-phase coupling.

Table 1 summarizes the frequency tuning coefficients of all actuators in the module. While the first four actuators are intended for controlling and tuning the optical emission frequency, varying I_{SOA} to change the optical output power of the laser module results in a parasitic cross-coupling to the emission frequency. The reason for this cross-coupling is Joule heating in the SOA chip, which heats up the MIOB. The resulting impact on the laser frequency is significantly reduced by active temperature stabilization of the MIOB at the position of its temperature sensor. However, depending on the location of the temperature sensor, this in turn can lead to a change in the effective length of the laser resonator. In order to further decrease the cross-coupling of I_{SOA} and further reduce the effects of additional environmental influences on the optical emission frequency (e.g., fluctuations in T_{HS}), an improved thermal stabilization concept of the MIOB with the use of multiple distributed temperature sensors would be beneficial.

The mode-hop-free frequency tuning range can be extended by tuning the optical resonator length and the center frequency of the VHBG at the same time. An active synchronization was achieved by utilizing the signals from the photodiodes PD-I and PD-T, which were amplified by two separate transimpedance

amplifiers (Thorlabs AMP102, 100 kHz) with 1 kOhm transimpedance gain. Dividing the photodiode voltage $V_{\text{PD-T}}$ by $V_{\text{PD-I}}$ results in an expression, which is proportional to the transmittance of the VHBG. Subtracting a constant c from the transmittance according to

$$e_1 = \frac{V_{\text{PD-T}}}{V_{\text{PD-I}}} - c, \quad (1)$$

results in an error signal e_1 , which can be used to stabilize the longitudinal laser mode to the transmittance slope of the VHBG. Figure 6 in the upper left corner shows the simulated transmittance of the VHBG as a function of the frequency deviation from the Bragg frequency. To facilitate implementation across a wide range of devices, particularly analog systems, we chose a different approach by transforming the error signal, allowing the two signals to be subtracted instead:

$$e_2 = V_{\text{PD-T}} - c \cdot V_{\text{PD-I}}. \quad (2)$$

Both methods yield identical results when the error signals are small. In order to examine the error signal for different injection currents, both photodiode voltages were measured using the analog input ports of the PTC10 temperature controller from SRS. As a proof-of-principle demonstrator, we chose a constant $c = 1.2$ to place the zero crossings on the slope of the VHBG's spectral response. Figure 6 shows the resulting error signal e_2 as a function of the ECDL injection current I_{ECDL} . Distinct zero transitions are observable, allowing the error signal e_2 to be used to stabilize the longitudinal laser mode to the slope of the VHBG by actively controlling I_{ECDL} , as shown in Fig. 2.

This control loop serves two purposes: frequency stabilization (will be discussed in Section 3.C) and mode-hop-free tuning. For the latter, we stabilized the longitudinal laser mode to the slope of the VHBG by controlling I_{ECDL} using a digital PID controller (Liquid Instruments Moku:Pro). When the VHBG temperature T_{VHBG} is varied, the error signal e_2 changes accordingly, but this is compensated by the PID controller through adjustments of I_{ECDL} , ensuring that the frequency of the longitudinal mode follows the central frequency of the grating.

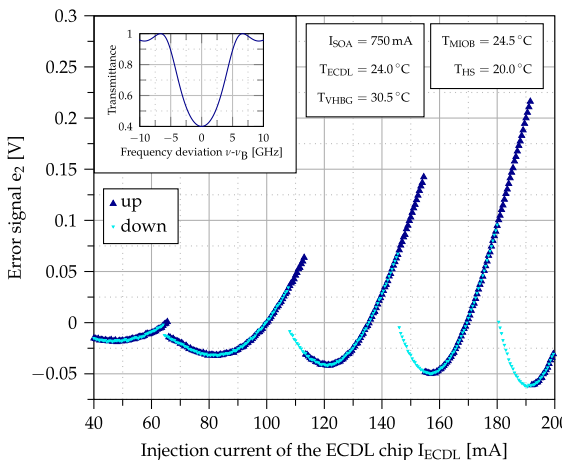


Fig. 6. Error signal e_2 of the VHBG spectroscopy versus the injection current of the ECDL chip I_{ECDL} and the simulated transmittance of the VHBG as a function of the frequency deviation from the Bragg frequency v_B .

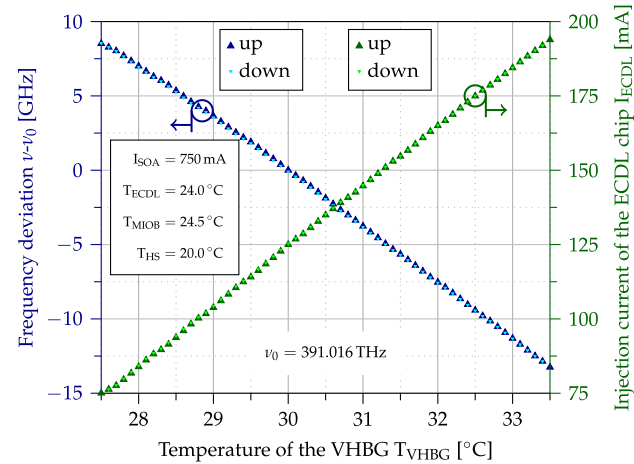


Fig. 7. Emission frequency v and the injection current of the ECDL I_{ECDL} of the ECDL-MOPA laser module as a function of the temperature of the VHBG T_{VHBG} , with the longitudinal laser mode stabilized to the slope of the VHBG by actively controlling I_{ECDL} . A mode-hop-free frequency tuning range of 22 GHz is achieved.

To demonstrate an extended mode-hop-free tuning range, the temperature T_{VHBG} was swept from 27.5°C to 33.5°C in 0.1°C steps in both directions, while the resulting injection current of the ECDL and the laser's emission frequency were recorded after each step. Figure 7 shows the results, demonstrating an extended mode-hop-free tuning range of 22 GHz. However, the maximum tuning range is constrained by the permitted injection current tuning range of the ECDL chip.

To extend the mode-hop-free frequency tuning range even further, an actuator with a higher frequency tuning range (T_{ECDL} or T_{MIOB}) has to be used instead of I_{ECDL} for active synchronization with T_{VHBG} . Figure 8 shows an extended mode-hop-free frequency tuning range of more than 100 GHz by employing a cascaded control loop, effectively utilizing I_{ECDL} for fast and T_{ECDL} for slow frequency changes. The tuning range of 100 GHz here is limited by the temperatures the ECDL chip can endure without reducing its lifetime. A temperature range of 19°C–30°C was used for demonstration purposes to achieve more than 100 GHz mode-hop-free tuning range. In both mode-hop-free tuning schemes, the fiber-coupled output power varied by about 10% ($\pm 5\%$), while the internal photodiode PD-SOA showed only 4% ($\pm 2\%$). This difference may arise from coupling efficiency drops or losses in the fiber setup (isolator and splitter).

To demonstrate a proof-of-principle implementation of a three-stage cascaded control loop, T_{MIOB} was included as an additional actuator to compensate for very slow frequency drifts. The transient behavior of this control loop is shown in Fig. 9. The activation of the controller prompted a rapid response in I_{ECDL} , with a time constant of approximately 500 μs, followed by the responses of T_{ECDL} and T_{MIOB} , with time constants of about 0.5 and 50 s, respectively. Due to its slower response and smaller tuning range compared to the Peltier element of the ECDL, the Peltier element of the MIOB is used primarily for long-term stabilization of the laser bench, while that of the ECDL enables faster frequency adjustments to follow environmental drifts such as temperature or pressure changes and

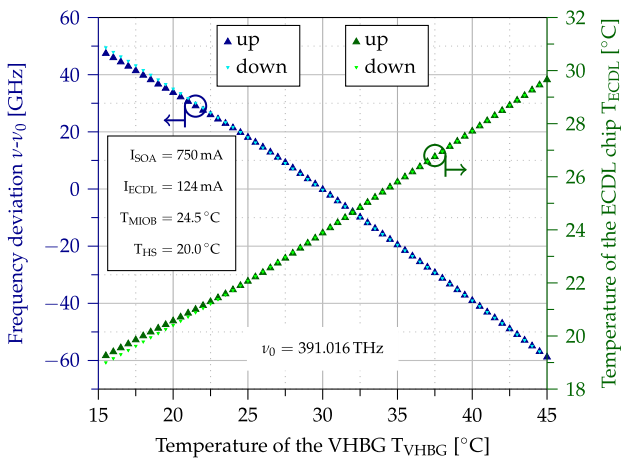


Fig. 8. Emission frequency ν and the temperature of the ECDL chip T_{ECDL} of the ECDL-MOPA laser module as a function of the temperature of the VHBG T_{VHBG} , with the longitudinal laser mode stabilized to the slope of the VHBG by employing a cascaded control loop, utilizing I_{ECDL} for fast frequency changes and T_{ECDL} for slow frequency changes. An extended mode-hop-free frequency tuning range of more than 100 GHz is achieved.

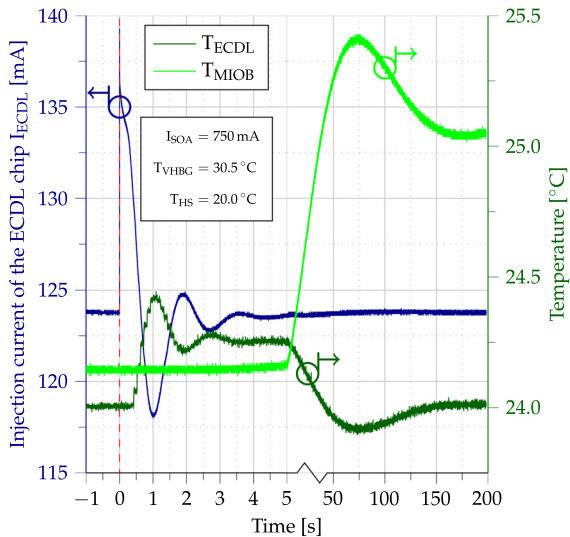


Fig. 9. Transient responses of I_{ECDL} , T_{ECDL} , and T_{MIOB} following the activation of the PID controller, which triggers a -2 GHz frequency jump, are shown. The injection current I_{ECDL} responds rapidly within approximately 500 μ s, while T_{ECDL} and T_{MIOB} exhibit slower thermal responses with time constants of about 0.5 and 50 s, respectively.

allows access to a broader tuning range than can be achieved by adjusting I_{ECDL} .

C. Spectral Stability

The spectral stability of the ECDL-MOPA module was investigated separately for both short-term and long-term stability. To analyze the short-term spectral stability of the ECDL-MOPA, an RF beat note signal was generated using a self-delayed ($\tau_D = 9994.5$ ns) heterodyne ($\Delta f_D = 93$ MHz) interferometer. Both quadrature components of the RF signal were captured

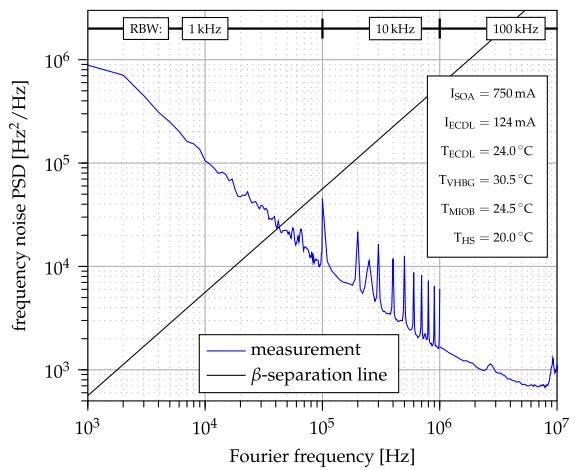


Fig. 10. Frequency noise power spectral density of the self-delayed heterodyne beat note measurement as a function of the Fourier frequency. The compensation of the interferometer's transfer function results in measurement artifacts appearing at integer multiples of τ_D^{-1} .

by an RF signal analyzer (Rohde & Schwarz FSW-26) with three different resolution bandwidths (RBW) to calculate the single-sided, double-sideband frequency noise power spectral density (PSD) ($S_f(f_F)$), which is shown in Fig. 10 as a function of the Fourier frequency. For a detailed explanation of this method, please refer to [34]. The compensation of the interferometer's transfer function results in measurement artifacts occurring at integer multiples of τ_D^{-1} . The background noise was measured separately and found to be below 5×10^0 Hz^2/Hz across the entire displayed Fourier frequency range. Since the white noise level is not reached within the measured range, only an upper limit for the intrinsic linewidth of the laser can be specified. The minimal frequency noise PSD of $S_f(f_F) = 680$ Hz^2/Hz corresponds to an intrinsic linewidth of $\Delta\nu_{\text{intrinsic}} = \pi \cdot S_f(f_F) = 2.1$ kHz. The technical linewidth was estimated using the β -separation line method [35], yielding 165 kHz at 1 ms timescales.

In order to analyze the long-term spectral stability, the light of the ECDL-MOPA and of a reference laser [a distributed feedback (DFB) laser] was superimposed to create an RF beat note signal. The beat note signal was detected by a high bandwidth (25 GHz) photodetector (New Focus 1434), followed by an RF amplifier (Centellax TA0L30VA), in order to measure its frequency in the RF domain with a frequency counter (Pendulum CNT-91R). The frequency of the reference laser was stabilized to the potassium D2 ground-state crossover transition ($\nu = 391.016230$ THz and $\Delta\nu \approx 6$ MHz). The ECDL-MOPA was free-running but operated with the longitudinal mode on the stabilization point on the VHBG by changing T_{VHBG} to 30.8 $^{\circ}$ C, to benefit from the frequency stabilization effect of amplitude-phase coupling. Dead-time free measurements of the beat note frequency over a time period of 7 days with a sampling interval of 1 s allowed the computation of the overlapping Allan deviation of the fractional frequency instability with a Python script using the AllanTools library [36] for time scales between 1 and 10^5 s.

The results are shown in blue in Fig. 11. The overall noise is dominated by white noise for timescales up to $\tau = 6$ s, leading

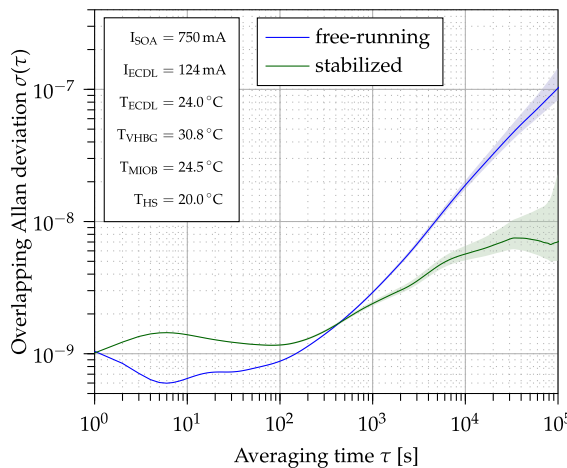


Fig. 11. Overlapping Allan deviation of the fractional frequency instability for free-running laser (blue) and the internally stabilized laser (green) as a function of the averaging times. The light blue and light green areas indicate the $1 - \sigma$ confidence intervals, which were calculated for drift dominating noise, of the overlapping Allan deviation calculation [37].

to improved frequency stability with increased averaging time. At an averaging time of $\tau = 6$ s, the minimum overlapping Allan deviation of $\sigma(\tau = 6\text{ s}) = 6 \cdot 10^{-10}$ is reached, indicating the highest stability of the emission frequency. On longer timescales, frequency stability is limited by linear drift, likely caused by environmental fluctuations in air pressure, relative humidity, and ambient temperature. However, the measured frequency instability might partially already be limited by the reference laser, as a comparable reference laser setup has demonstrated Allan deviations of 2×10^{-10} at 1 s and a minimum of 7×10^{-11} at 16 s [23].

The same measurement was conducted for the case when the ECDL-MOPA was stabilized on its internal VHBG over a time period of 2 days, using the aforementioned error signal e_2 and an actively controlled I_{ECDL} . The result is shown in green in Fig. 11. The internally stabilized ECDL-MOPA (green) exhibits a slightly higher Allan deviation for timescales up to $\tau = 500$ s, due to injected noise from the control electronics. However, the key benefit of internally stabilizing the laser manifests itself on longer timescales, yielding up to an order of magnitude reduction in the influence of drift [i.e., from $\sigma(\tau = 10^5\text{ s}) = 10^{-7}$ to $\sigma(\tau = 10^5\text{ s}) = 7 \cdot 10^{-9}$]. The remaining drift is a consequence of center frequency fluctuations of the VHBG, presumably caused by thermal radiation onto the top side of the VHBG. Further improvements are plausible by thermally isolating the Bragg grating.

D. Spectral Purity

Lastly, the spectral purity of the ECDL-MOPA module was investigated by measuring its spectrum with an RF signal analyzer (Rohde & Schwarz FSW-26) with a 3 MHz resolution bandwidth. This was possible by superimposing the ECDL-MOPA laser beam with the beam of a free-running DFB diode laser to generate a beat note signal in the RF domain. A high-bandwidth (25 GHz) photodetector (New Focus 1434), followed by an RF amplifier (Centellax TA0L30VA), was used

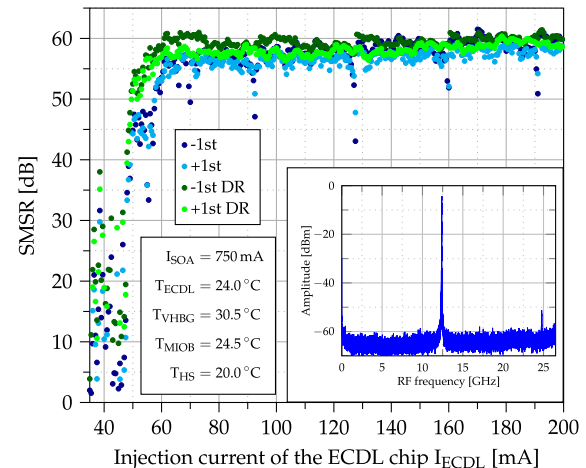


Fig. 12. Side mode suppression ratio for the lower frequency (-1st) and higher frequency ($+1\text{st}$) side mode as a function of the injection current of the ECDL chip. The inset shows the spectrum at the operating point. The spectrum was measured with a 3 MHz resolution bandwidth.

to detect the signal. The DFB laser diode was operated at constant injection current and temperature to keep its frequency stable. I_{ECDL} was swept to calculate the side mode suppression ratio (SMSR) of the lower frequency (-1st) and higher frequency ($+1\text{st}$) side mode for different operating conditions. Figure 12 shows the SMSR and the dynamic range (DR) (distance between the carrier level and the noise background) as a function of I_{ECDL} and the spectrum in the middle of a mode at $I_{\text{ECDL}} = 110$ mA. The spectrum at the operating point reveals a single peak, indicating strong suppression of side modes. Above the threshold current, the SMSR of the laser exceeds 42 dB and reaches more than 55 dB throughout the swept injection current range. The clearly visible minima of the SMSR, roughly every 40 mA, are attributed to mode-hops.

4. SUMMARY AND OUTLOOK

We presented a robust and compact hybrid micro-integrated, narrow-linewidth laser module for quantum technology applications. The laser module employs an ECDL and an RWA as master oscillator and power amplifier, respectively, allowing for independent tuning of the emission frequency and output power.

The ECDL-MOPA module features a metallic micro-optical bench made of an $\text{Mo}_{70}\text{Cu}_{30}$ alloy, ensuring high thermal conductivity and low CTE mismatch with the GaAs chips. The MIOB's top side contains all optical and electro-optical components, including three photodiodes for optical power monitoring. In addition, two Peltier elements for temperature stabilization and tuning of both the VHBG and the ECDL chip are also integrated on the top side. The MIOB is encased in an aluminum housing and is temperature stabilized using four additional Peltier elements mounted inside the housing.

Various actuators (I_{ECDL} , T_{ECDL} , T_{MIOB} , and T_{VHBG}) allow for tuning the optical emission frequency with different dynamic ranges and time constants. We demonstrate a

mode-hop-free frequency tuning range of 22 GHz, extendable beyond 100 GHz using a cascaded control loop. The error signal for stabilization is derived from spectroscopy of the frequency-selective element, monitored via two photodiodes. The free-running module reaches a high level of spectral stability with a technical linewidth of approximately 165 kHz at 1 ms and a minimum overlapping Allan deviation of $\sigma(\tau = 6 \text{ s}) = 6 \cdot 10^{-10}$. An improvement of the frequency stability on time scales exceeding 500 s was achieved by stabilizing the laser on its internal VHBG, which led to a reduction of frequency drifts by up to one order of magnitude [i.e., from $\sigma(\tau = 10^5 \text{ s}) = 10^{-7}$ to $\sigma(\tau = 10^5 \text{ s}) = 7 \cdot 10^{-9}$].

The hybrid micro-integrated ECDL-MOPA laser module's robust design and thermal management ensure reliable operation in various environments—in the field and in space. Combined with its extended mode-hop-free tuning range, high optical output power, and high spectral stability, this paves the way for further developments in quantum technologies.

Funding. Bundesministerium für Bildung und Forschung (13N15724, 13N14906); Bundesministerium für Wirtschaft und Energie (50WM2053, 50WM2152, 50WM2176, 50WM2164, 50WM2351C); European Regional Development Fund (10168115).

Acknowledgment. This work was supported by the DLR Space Administration with funds provided by the Federal Ministry for Economic Affairs and Energy under grant numbers 50WM2053, 50WM2152, 50WM2176, 50WM2164, and 50WM2351C; by VDI Technologiezentrum GmbH with funds provided by the Federal Ministry of Research, Technology, and Space within the funding program “Quantum technologies—from basic research to market” under grant number 13N15724 and within the funding program Photonics Research Germany under grant number 13N14906; and by Investitionsbank Berlin with funds provided by the European Union under grant number 10168115.

Disclosures. The authors declare no conflicts of interest.

Data availability. Data underlying the results presented in this paper are not publicly available at this time but may be obtained from the authors upon reasonable request.

REFERENCES

- R. Geiger, V. Ménoret, G. Stern, et al., “Detecting inertial effects with airborne matter-wave interferometry,” *Nat. Commun.* **2**, 474 (2011).
- N. Yu, J. Kohel, J. Kellogg, et al., “Development of an atom-interferometer gravity gradiometer for gravity measurement from space,” *Appl. Phys. B* **84**, 647–652 (2006).
- K. Herb, L. A. Völker, J. M. Abendroth, et al., “Quantum magnetometry of transient signals with a time resolution of 1.1 nanoseconds,” *Nat. Commun.* **16**, 822 (2025).
- M. T. Simons, J. A. Gordon, C. L. Holloway, et al., “Using frequency detuning to improve the sensitivity of electric field measurements via electromagnetically induced transparency and Autler-Townes splitting in Rydberg atoms,” *Appl. Phys. Lett.* **108**, 174101 (2016).
- A. D. Ludlow, M. M. Boyd, J. Ye, et al., “Optical atomic clocks,” *Rev. Mod. Phys.* **87**, 637–701 (2015).
- LIGO Scientific Collaboration and Virgo Collaboration, “Observation of gravitational waves from a binary black hole merger,” *Phys. Rev. Lett.* **116**, 061102 (2016).
- T. van Zoest, N. Gaaloul, Y. Singh, et al., “Bose-Einstein condensation in microgravity,” *Science* **328**, 1540–1543 (2010).
- M. Schiemangk, K. Lampmann, A. Dinkelaker, et al., “High-power, micro-integrated diode laser modules at 767 and 780 nm for portable quantum gas experiments,” *Appl. Opt.* **54**, 5332–5338 (2015).
- A. Wicht, A. Bawamia, M. Krüger, et al., “Narrow linewidth diode laser modules for quantum optical sensor applications in the field and in space,” *Proc. SPIE* **10085**, 100850F (2017).
- C. Kürbis, A. Bawamia, M. Krüger, et al., “Extended cavity diode laser master-oscillator-power-amplifier for operation of an iodine frequency reference on a sounding rocket,” *Appl. Opt.* **59**, 253–262 (2020).
- L. Prade, A. Selyem, B. Jones, et al., “Optimised tapered amplifier systems for quantum technologies,” *Proc. SPIE* **11295**, 112950L (2020).
- R. I. Tobey, K. W. Lee, A. M. Hankin, et al., “A high-power, low-noise, ultraviolet laser system for trapped-ion quantum computing,” in *Conference on Lasers and Electro-Optics (CLEO)* (2020), pp. 1–2.
- A. Bachmann, M. v. Sivers, C. Nölleke, et al., “High-power diode lasers for quantum technologies,” *Proc. SPIE* **12867**, 1286714 (2024).
- V. V. Vassiliev, S. A. Zibrov, and V. L. Velichansky, “Compact extended-cavity diode laser for atomic spectroscopy and metrology,” *Rev. Sci. Instrum.* **77**, 013102 (2006).
- A. N. Dinkelaker, M. Schiemangk, V. Schkolnik, et al., “Autonomous frequency stabilization of two extended-cavity diode lasers at the potassium wavelength on a sounding rocket,” *Appl. Opt.* **56**, 1388–1396 (2017).
- E. Luvsandambin, C. Kürbis, M. Schiemangk, et al., “Micro-integrated extended cavity diode lasers for precision potassium spectroscopy in space,” *Opt. Express* **22**, 7790–7798 (2014).
- C. Raab, A. Able, and R. Heidemann, “Method for stabilizing a diode laser,” U.S. patent 9,960,569B2 (1 May 2018).
- R. Neuhaus, “TOPTICA Photonics, Inc.: simple operation of a continuously tunable laser with up to 120nm mode-hop free tuning range,” *Proc. SPIE* **11716**, 117162C (2021).
- K. S. Repasky, A. R. Nehrir, J. T. Hawthorne, et al., “Extending the continuous tuning range of an external-cavity diode laser,” *Appl. Opt.* **45**, 9013–9020 (2006).
- Y.-G. Sun, F. Wei, D.-J. Chen, et al., “Design of a mode-hop-free tunable external cavity diode laser with a PLZT electro-optic ceramic deflector,” *Proc. SPIE* **8192**, 81923I (2011).
- A. Zhang, S. Qiao, L. Sheng, et al., “Study on external cavity diode laser with a wide mode-hopping free tuning range,” *Front. Phys.* **10**, 1093179 (2022).
- J. Sun, L. Qiu, L. Liu, et al., “Output characteristics of external-cavity mode-hop-free tunable laser source in C+L band,” *Photonics* **11**, 677 (2024).
- J. Pahl, A. N. Dinkelaker, C. Grzeschik, et al., “Compact and robust diode laser system technology for dual-species ultracold atom experiments with rubidium and potassium in microgravity,” *Appl. Opt.* **58**, 5456–5464 (2019).
- M. Bocheński, J. Dobosz, and M. Semczuk, “Magnetic trapping of an ultracold ^{39}K - ^{40}K mixture with a versatile potassium laser system,” *Opt. Express* **32**, 48463–48478 (2024).
- D. Zou, M. Schiemangk, C. Tyborski, et al., “Low-stress optical bench with thermal decoupling,” German patent DE 10,2023,111,589 B3 (1 August 2024).
- H. Kogelnik, “Coupled wave theory for thick hologram gratings,” *Bell Syst. Tech. J.* **48**, 2909–2947 (1969).
- J. M. Baumann, J. Strobelt, C. Kürbis, et al., “Influence of feedback on master oscillator power amplifier laser systems with external-cavity diode lasers for quantum experiments in space,” *Proc. SPIE* **13699**, 1369935 (2025).
- C. Tyborski, M. T. Hassan, T. Flisgen, et al., “Extensive study of magneto-optical and optical properties of $\text{Cd}_{1-x}\text{Mn}_x\text{Te}$ between 675 and 1025 nm,” *AIP Adv.* **13**, 015213 (2023).
- M. Bursy, A. Bawamia, T. Flisgen, et al., “Miniaturised optical isolators for realising micro-integrated photonic modules in quantum technology applications,” in *Conference on Lasers and Electro-Optics Europe & European Quantum Electronics Conference (CLEO/Europe-EQEC)* (2025), p. 1.
- S. S. Saini, S. H. Cho, and M. Dagenais, “Thermal considerations in high power semiconductor lasers and semiconductor optical amplifiers,” *Proc. SPIE* **6478**, 647805 (2007).
- J. R. Andrews, “Variable focusing due to refractive-index gradients in a diode-array traveling-wave amplifier,” *J. Appl. Phys.* **64**, 2134–2137 (1988).
- C. L. Tang, H. Statz, and G. deMars, “Spectral output and spiking behavior of solid-state lasers,” *J. Appl. Phys.* **34**, 2289–2295 (1963).

33. K. Petermann, *Laser Diode Modulation and Noise*, 1st ed. (Springer, 1988).
34. M. Schiemangk, S. Spießberger, A. Wicht, et al., "Accurate frequency noise measurement of free-running lasers," *Appl. Opt.* **53**, 7138–7143 (2014).
35. G. Di Domenico, S. Schilt, and P. Thomann, "Simple approach to the relation between laser frequency noise and laser line shape," *Appl. Opt.* **49**, 4801–4807 (2010).
36. A. E. E. Wallin, D. C. Price, C. G. Carson, et al., "allantools: Allan deviation calculation," Astrophysics Source Code Library (2018), <https://ui.adsabs.harvard.edu/abs/2018ascl.soft04021W/abstract>.
37. C. A. Greenhall and W. J. Riley, "Uncertainty of stability variances based on finite differences," in *Proceedings of the 35th Annual Precise Time and Time Interval Systems and Applications Meeting* (2003), pp. 267–280.